Atomic ordering in nanosized Pt_xAu_{1-x} ($x = 0, 0.51, 1$) by resonant X-ray diffraction and differential atomic pair distribution functions

Valeri Petkov[*, I], Sarvjit Shastri[II], Bridgid Wanjala[III], Rameshiwori Loukrakpam[III], Jin Luo[III] and Chuan-Jian Zhong[III]

[I] Department of Physics, Central Michigan University, Mt. Pleasant, MI 48859, USA
[II] Advanced Photon Source, Argonne National Laboratory, Argonne, IL 60439, USA
[III] Department of Chemistry, State University of New York at Binghamton, Binghamton, New York 13902, USA

Abstract. Resonant X-ray diffraction and differential atomic pair distribution functions method is illustrated with results from a study of 4.5(3) nm Pt, Au and $Pt_{0.51}Au_{0.49}$ particles. By doing experiments at two energies close to the *K* absorption edge of Pt the atomic correlations relative to Pt and Au atoms in the alloy particles are differentiated. The experimental data show that Pt and Au atoms in all three samples arrange in a face centered cubic type structure while keeping their bond lengths of 2.76 Å and 2.86 Å, respectively, virtually unchanged. This leads to increased local structural distortions in the alloyed $Pt_{0.51}Au_{0.49}$ particles that may affect their catalitic properties substantially.

Introduction

Atoms in bulk crystalline materials are arranged in a periodic pattern over long-range (μm-scale or longer) distances. That is why their atomic-scale structure can be conveniently described and properties explained in terms of periodic, *i.e.* deemed infinite lattices – 14 in number [1]. When an arrangement of atoms sitting on the vertices of one of these (Bravais) lattices is irradiated with X-rays, it acts as a perfect diffraction grating and so produces a diffraction pattern showing numerous sharp spots, called Bragg diffraction peaks. By measuring and analyzing the positions and intensities of those peaks it is possible to determine the spatial characteristics of the periodic lattice/grating, *i.e.* to determine the atomic-scale structure of the respective crystalline material. This is the essence of the so-called crystal structure determination by Bragg X-ray diffraction [2]. Many materials of current scientific and technological interest, such as crystals with local topological and/or chemical disorder, nanosized particles (NP)s, composites, glasses, and others do not exhibit a periodic, long-range atomic structure. As a result, when irradiated with X-rays they act as gratings of limited structural co-herence and show diffraction patterns with a few Bragg-like peaks, if any, and a strong diffuse component. The interpretation of such diffraction patterns within the formalism of traditional Bragg crystallography is hardly possible. A non-traditional approach involving high-energy X-ray or neutron diffraction and atomic Pair Distribution Function (PDF) analysis has proven much better suited to the task [3–5].

In brief, the frequently used reduced atomic PDF, $G(r)$, gives the number of atoms in a spherical shell of unit thickness at a distance *r* from a reference atom as follows:

$$G(r) = 4\pi r[\varrho(r) - \varrho_0] \qquad (1)$$

where $\varrho(r)$ and ϱ_0 are the local and average atomic number densities, respectively. As defined, the PDF $G(r)$ is a one-dimensional function that oscillates around zero showing positive peaks at distances separating pairs of atoms while the areas under the peaks are proportional to the number of atomic pairs at those distances. With this respect the PDF resembles the so-called Patterson function that is widely used in traditional crystallography [2]. However, while the Patterson function is discrete and peaks at interatomic distances within the unit cell of a crystal, the atomic PDF is a continuous function peaking at all interatomic distances in a material. This is a great advantage when studying materials where atoms do not necessarily sit on the vertices of unit cells of infinitely periodic lattices. The PDF $G(r)$ is the Fourier transform of the experimentally observable total structure function, $S(q)$, *i.e.*

$$G(r) = (2/\pi) \int_{q=0}^{q_{max}} q[S(q) - 1] \sin(qr)\,dq, \qquad (2)$$

where q is the magnitude of the wave vector ($q = 4\pi \sin\theta/\lambda$), 2θ is the angle between the incoming and outgoing X-rays and λ is the wavelength of the X-rays used. X-ray diffraction (XRD) usually employs the so-called Faber-Ziman type structure function, $S(q)$, related to the coherent part of the diffraction pattern, $I^{coh}(q)$, as follows:

$$S(q) = 1 + [I^{coh}(q) - \sum c_i|f_i(q)|^2]/|\sum c_i f_i(q)|^2, \qquad (3)$$

* Correspondence author (e-mail: petkov@phy.cmich.edu)

where c_i and $f_i(q)$ are the atomic concentration and X-ray scattering factor respectively for the atomic species of type i. A single high-energy XRD experiment, however, yields a PDF which is a weighted sum of the contributions of the partial correlations between all distinct atomic pairs that are $n(n+1)/2$ in number for a material composed of n atomic species, i.e.

$$G(r) = \sum_{i,j} w_{ij} G_{ij}(r), \qquad (4)$$

where $G_{ij}(r)$ are the so-called partial PDFs. Here w_{ij} are weighting factors depending on the concentration and scattering power of the particular atomic species as follows:

$$w_{ij} = c_i c_j f_i(Q) f_j(Q) / [\sum c_i f_i(Q)]^2. \qquad (5)$$

This can make ambiguous the interpretation of PDF data, especially in the case of multielement materials. Element specificity may be added by employing the so-called resonant XRD, which involves measuring two diffraction data sets close to but below the absorption edge of an atomic species, taking the difference between these two data sets, and Fourier transforming it into a quantity called a differential atomic PDF [6, 7]. Similarly to Extended X-ray Absorption Fine Structure (EXAFS) spectroscopy, the differential atomic PDF will reflect only correlations relative to the element whose absorption edge is probed. However, unlike EXAFS, it will show these correlations to the longest interatomic distances to which they extend in the material under study. The approach has been successfully applied to glasses, liquids [6, 7] and recently to NPs [8, 9]. Here we illustrate its great potential in a study of 4.5(3) nm Pt_xAu_{1-x} ($x = 0, 0.51, 1$) particles being explored for catalytic applications [10, 11]. The enhanced catalytic activity of Pt−Au NPs has been attributed to alloying and structural distortion effects [11–15] though a complete understanding why Pt and Au are inert as bulk crystals but catalytically very active when nanosized and alloyed is still lacking.

Experimental

Sample preparation

Gold (Au), Platinum (Pt) and gold-platinum alloy (AuPt) nanoparticles were synthesized by a modified two-phase method. It involved transferring of $AuCl_4$ and $PtCl_6$ from aqueous solution of $HAuCl_4$ and H_2PtCl_6 into toluene using tetraoctylammonium bromide as a phase-transfer reagent. Thiols or amine compounds were added to the organic solution as NPs capping agents. An excess of aqueous $NaBH_4$ was slowly added for the reduction reaction. The resulting NPs were collected by removing the toluene solvent, washed in ethanol, and redispersed in hexane. Carbon black obtained from Cabot was used as NP's support. The carbon black was first pretreated by suspending in hexane and sonicated for 6 h at room temperature. A controlled amount of Au, Pt or AuPt alloy nanoparticles was added into the suspension. The suspension was sonicated for another 30 min, followed by stirring overnight.

Thus prepared carbon-supported Au, Pt and AuPt particles were collected and dried under N_2. The carbon-supported NPs were annealed in a tube furnace at 300 °C under 20% O_2/N_2 for 1 h and then at 400 °C under 15% H_2/N_2 atmosphere for extra 2 h. Note that the treatment conditions adopted here were found to result in very active NPs catalysts [10, 11]. The exact Au, Pt and AuPt NP's compositions were determined by direct current plasma-atomic emission spectroscopy and found to be Au, Pt and $Pt_{0.51}Au_{0.49}$. TEM studies showed that the NPs are spherical in shape and with a narrow size distribution centered at 4.5(3) nm. The carbon-supported NPs were loaded into thin-walled glass capillaries with a diameter of 1.5 mm and subjected to XRD experiments.

High-energy resonant X-ray diffraction experiments

XRD experiments were carried out at the 1-ID beamline of the Advanced Photon Source at the Argonne National Laboratory. All three samples were measured with X-rays of energy 78.070 keV which is 325 eV below the K absorption edge of Pt. A pure carbon sample not loaded with NPs was also measured and used as a reference "background" sample. In addition the $Pt_{0.51}Au_{0.49}$ NPs sample was measured with X-rays of energy 78.370 keV that is 25 eV below the K adsorption edge of Pt (see Fig. 1). The beam was delivered by a combination of a bent double-Laue premonochromator, collimating refracting lenses and a four crystal high-energy resolution ($\Delta E = 8$ eV) monochromator [16]. The monochromator set-up was calibrated and occasionally checked during data collection for stability against sub-eV energy drifts using the K absorption edge of a pure Pt foil in transmission. Scattered X-rays were collected by a single, intrinsic Ge detector coupled to a multichannel analyzer. Few energy windows, covering several neighboring channels, were set up to obtain counts integrated over specific X-ray energy ranges during the data collection. These energy windows covered: the elastic/coherent intensity only (see the broken line marked areas in Fig. 2); the elastic, inelastic/incoherent (Compton), and PtK_β fluorescence intensities all together; the $PtK_{\alpha1}$ and $K_{\alpha2}$ fluorescence; and the
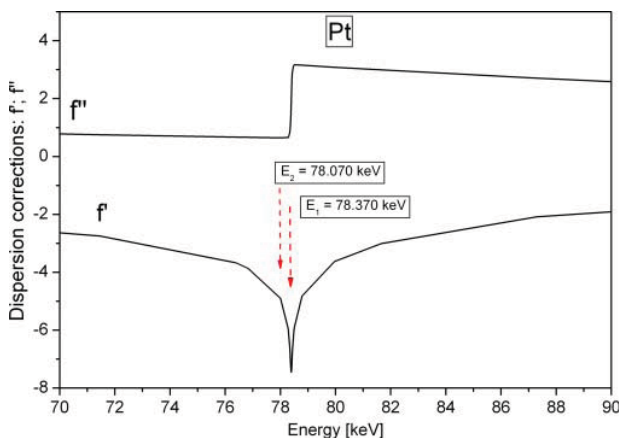

Fig. 1. Energy dependence of the real f' and imaginary f'' dispersion corrections to the X-ray scattering factor of Pt. The energies below the Pt K edge used in the present experiment are marked with arrows.
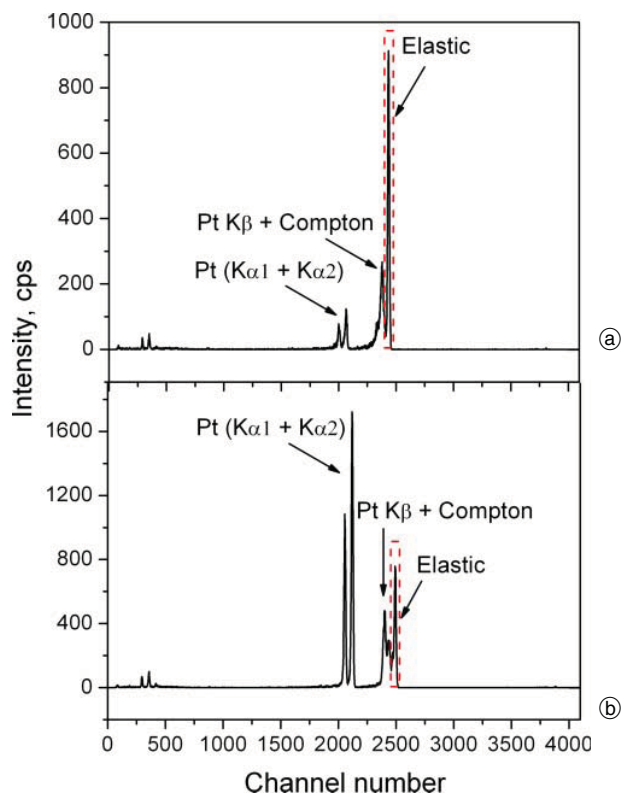
Fig. 2. Scattered intensities vs multi-channel analyzer number taken at a fixed wave vector, q, of 20 Å^{-1} with X-rays of energy 78.070 keV (**a**) and 78.370 keV (**b**). The intensity of the elastically scattered photons (marked with a broken line in red) greatly diminishes and that of the fluorescent radiation ($K_{\alpha 1}$, $K_{\alpha 2}$ and K_{β}) increases when the data are taken closer (*i.e.* at 78.370 keV) to the Pt K absorption edge.

Fig. 3. (**a**) Experimental XRD patterns for 4.5 nm Pt$_{0.51}$Au$_{0.49}$ particles measured with X-rays of 78.070 keV (black) and 78.370 keV (red) energy. The difference (in cyan) between the two data sets is shown at the lower part of the plot. In the inset the 78.070 keV data set is shown again this time with the XRD pattern of pure carbon used as a support of the particles. (**b**) Total (single energy of 78.070 keV X-ray photons) and Pt differential reduced structure functions $q[S(q) - 1]$ extracted from the data sets shown in (**a**).

total intensity scattered into the Ge detector. Integrated counts within these ranges were collected several times scanning up to wave vectors of 24 Å^{-1} and then averaged to improve the statistical accuracy. The integrated range of only elastically scattered X-ray photons with energy of 78.070 keV was further corrected for detector dead time, sample absorption and background/pure carbon scattering. The latter appeared quite weak (see the inset in Fig. 3a) as compared to the scattering from the NPs due to the much weaker scattering power of carbon atoms (atomic number $Z = 6$) as compared to that of Pt and Au atoms (with atomic numbers $Z = 78$ and 79, respectively). The contribution of sample's fluorescent and inelastic scattering (see Fig. 2) need not be corrected for since it was conveniently eliminated during data collection thanks to the usage of an energy sensitive Ge detector. Note the latter correction is often of a major concern in atomic PDF experiments since it is only the coherent/elastic part of the X-ray scattered intensities that is relevant to the atomic PDFs derivation (see Eqs. (2) and (3)). The so corrected XRD data was reduced to structure factors Eq. (3) and then Fourier transformed Eq. (2) to the atomic PDFs shown in Fig. 4a. Note thus derived atomic PDFs are usually called total in a sense that they show all distinct types of interatomic correlations in the respective materials. For the Au and Pt NPs the total PDFs thus reflect the correlations between the only one type of chemical species: Au−Au and Pt−Pt
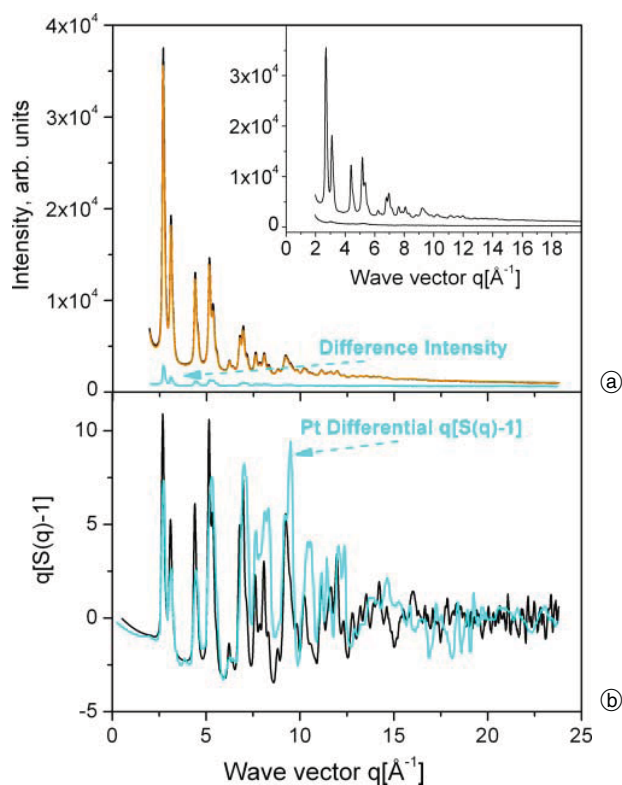
correlations, respectively. For the Pt$_{0.51}$Au$_{0.49}$ NPs the total PDF reflects the correlations between the two types of chemical species present, *i.e.* Au−Au, Au−Pt and Pt−Pt correlations.

Next, only the elastically scattered from the Pt$_{0.51}$Au$_{0.49}$ sample intensities collected with 78.370 keV X-rays were subtracted out from the elastically scattered intensities collected with 78.070 keV X-rays. The difference intensity is quite substantial as shown in Fig. 3a. The reason is that 78.370 keV energy photons excite much stronger the fluorescence of Pt atomic species than the 78.070 keV energy photons since the former are much closer to the Pt K absorption edge than the latter (see Fig. 1). As a result more X-ray photons appear as $K_{\alpha 1}$, $K_{\alpha 2}$ and Pt K_{β} lines and less are elastically (*i.e.* with an unmodified energy) scattered in the former data set than in the latter (see Fig. 2). The difference intensity was used to derive the so-called differential structure factor [6–8],

$$DS(q)_{\text{Pt}}$$
$$= \frac{I^{\text{coh}}(q, E_1) - I^{\text{coh}}(q, E_2) - [\langle f^2(E_1) \rangle - \langle f^2(E_2) \rangle]}{\langle f(E_1) \rangle^2 - \langle f(E_2) \rangle^2} + 1$$
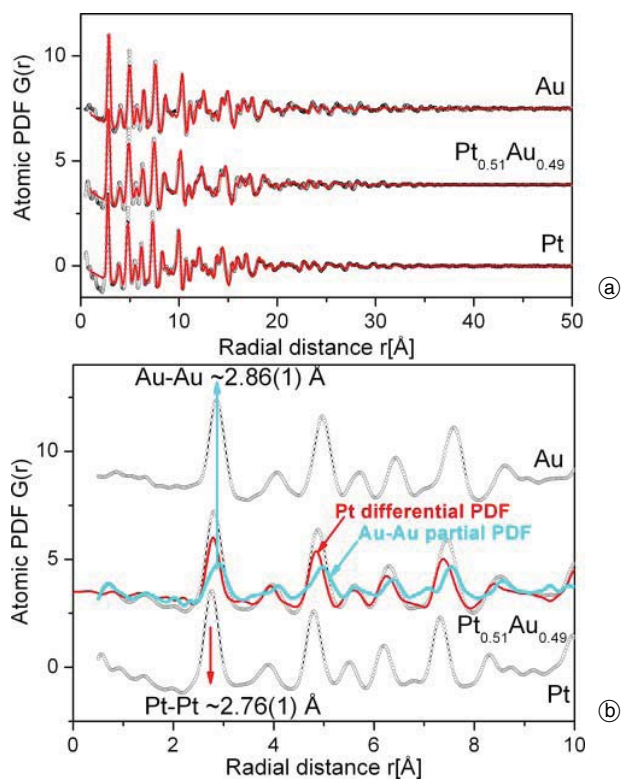
$$(6)$$

Fig. 4. Experimental (line in black/symbols) and model (line in red) total atomic PDFs for 4.5 nm Au, Pt and $Pt_{0.51}Au_{0.41}$ NPs shifted by a constant for clarity (**a**). Low-r part of the total atomic PDFs together with the experimental Pt differential (line in red) and Au−Au (line in cyan) partial PDFs for $Pt_{0.51}Au_{0.41}$ NPs (**b**). Arrows mark the positions of Pt−Pt and Au−Au first coordination spheres/bond lengths.

where E_1 and E_2 denote the data sets collected with X-rays of 78.070 keV and 78.370 keV energy, respectively, and the atomic scattering factors $f(E) = f_o(q) + f'(q,E) + if''(q,E)$ are evaluated with the respective for the two energies dispersion corrections f' and f'' [8]. Note in the derivation of $DS(q)$ the $I^{coh}(q,E_1)$ and $I^{coh}(q,E_2)$ data sets need not necessarily be subjected to prior correction for background/pure carbon scattering since it naturally cancels out in their difference. The corresponding Pt differential atomic PDF, $DG(r)A$, was obtained via a Fourier transformation as follows:

$$DG(r)_{Pt} = \frac{2}{\pi} \int_{q=0}^{q_{max}} q[DS(q)_{Pt} - 1] \sin(qr)\, dq \qquad (7)$$

where q_{max} extends to 24 Å^{-1}. Note, since only the scattering form factor of Pt atoms changed significantly, the differential atomic PDF contains contributions from atomic pairs involving Pt-i type atoms only, $i.e.$:

$$DG(r)_{Pt} = \sum_i \Delta w_{Pt-i}\, G_{Pt-i}(r) \qquad (8)$$

where

$$\Delta w_{Pt-i} = \frac{c_{Pt} c_i \, \text{Re} \, [f_i(f^*_{Pt}(E_1) - f^*_{Pt}(E_2)]}{\langle f(E_1) \rangle^2 - \langle f(E_2) \rangle^2}, \qquad (9)$$

$f^*(E)$ is the complex conjugate of $f(q)$ and $i = $ Pt, Au [8]. The as obtained Pt differential structure factor is shown in Fig. 3b. Its Fourier transform, the so-called Pt differential atomic PDF, that reflects Pt−Pt and Pt−Au correlations only, is shown in Fig. 4b. Furthermore, by using the MIXSCAT approach [17] the Au−Au correlations in the $Pt_{0.51}Au_{0.49}$ NPs were also obtained from the experimental total PDF and Pt differential PDF data. Basically the MIXSCAT approach involves appropriately weighing two experimental atomic PDFs and taking a difference between them to eliminate particular atomic pair correlations that appear in the two PDFs but with different weight contributions ($e.g.$ see Eq. (8) in Ref. [17]). Following the MIXSCAT approach the Pt−Pt and Pt−Au correlations in $Pt_{0.51}Au_{0.49}$ NPs were eliminated and the Au−Au correlations extracted as follows:

Au−Au partial PDF

$$= (\text{our Total } G(r))/w_{ij} - (\text{our } DG(r)_{Pt})/\Delta w_{Pt-i} \qquad (10)$$

where w_{ij} and Δw_{Pt-i} are the weighting factors of the Pt−Pt and Pt−Au atomic pairs estimated using the respective definitions given in Eqs. (5) and (9) above. Note the derivation of the Au−Au partial PDF by Eq. (10) is relatively straightforward in our case since both experimental PDF data sets involved in it have been derived from XRD data collected on the same instrument with similar statistical accuracy and to the same Q_{max} value, and have also been subjected to analogous correction and Fourier transformation protocols. The resulting Au−Au partial atomic PDF for 4.5(3) nm $Pt_{0.51}Au_{0.49}$ NPs is also shown in Fig. 3b. Thus by conducting two high-energy XRD experiments close to the Pt K absorption edge structure data sensitive not only to the atomic ordering but specific to the chemistry of $Pt_{0.51}Au_{0.49}$ alloy NPs were obtained.

Results and discussion

As can be seen in Fig. 4a, the total PDFs show a series of sharp peaks reflecting the presence of well defined atomic coordination spheres in the NPs studied here. For 4.5(3) nm particles of perfect crystallinity the respective total PDFs should show physical oscillations up to distances of 4.5 nm. The experimental PDFs, however, decay to zero at distances of about 3.5 nm which indicates the presence of local structural disorder diminishing the NP's structural coherence length to distances shorter than their size. Noble metals based NPs are often found to show such disorder mostly due to surface relaxation effects [18, 19]. The total PDFs for Pt and Au NPs have their first peaks positioned at distances of 2.76(1) Å and 2.86(1) Å which are very close to the Pt−Pt and Au−Au bond lengths in bulk Pt and Au, respectively. The first peak in the total PDF for $Pt_{0.51}Au_{0.49}$ is positioned at about 2.80(1) Å which may be interpreted as an "average" metal−metal atom bond length (metal = Pt, Au) in these NPs. The eventual presence of fine structure in that peak, $i.e.$ the eventual presence of distinct Pt−Pt and Au−Au bond lengths, may not be resolved in the present total PDFs since the q_{max} of the XRD data is 24 Å^{-1} limiting

the real space resolution ($\Delta r = 2\pi/q_{max}$) to approximately 0.25 Å. The experimental total PDFs may be approximated very well (see the red lines in Fig. 4a) with a model based on a face centered cubic (fcc)-type atomic ordering occurring in bulk Pt and Au. In this type of Bravais lattices based modeling a PDF for an infinite fcc lattice is first computed. Then each of the coordination spheres of the perfect lattice is broadened by a convolution with a gaussian function to take into account the presence of thermal (Debye-Waller type [2]) and static local atomic displacements in real NPs. At the same time the computed PDF is multiplied by a particle shape (spherical in our case) dependent function which is zero for distances longer than the size of the NPs being modeled. It is a simplistic approximation to the structure of real NPs but is useful since it allows i) to verify the type of their atomic ordering and ii) obtain a set of structural parameters (*e.g.* lattice constants and atomic displacement amplitudes) that may be compared directly with those for the corresponding bulk materials. The computations were done with the help of the program PDFgui [20]. Thus obtained "lattice" parameters for Pt, Au and $Pt_{0.51}Au_{0.49}$ NPs are 3.92(1) Å, 4.07(1) Å and 3.99(1) Å, respectively. For reference the lattice parameter of bulk fcc Pt is 3.924 Å and that for bulk fcc Au – 4.080 Å. No lattice parameter for bulk $Pt_{0.51}Au_{0.49}$ is known since Pt and Au are immiscible in bulk. The result shows that atoms in all NPs studied here exhibit a similar, fcc-type atomic ordering. The PDFgui modeling also yielded an "average" root-mean-square (rms) displacement amplitudes of 0.016(1) Å, 0.016(1) Å and 0.023(1) Å for the atoms in Pt, Au and $Pt_{0.51}Au_{0.49}$ NPs, respectively. Obviously atoms in the $Pt_{0.51}Au_{0.49}$ NPs suffer extra, *i.e.* beyond the usual thermal and surface relaxation induced structural disorder, and disorder is known to affect the catalytic properties of metallic NPs very substantially [21].

To understand the origin of the extra structural disorder in $Pt_{0.51}Au_{0.49}$ NPs we turn our attention to the resonant XRD derived data. As can be seen in Fig. 4b the Pt differential PDF has its first peak at a distance close to the Pt-Pt bond length in pure Pt. Furthermore, the Au−Au partial PDF has its first peak at a distance very close to the Au-Au bond length in pure Au. The result shows that Pt−Pt and Au−Au bond lengths in 4.5(3) nm carbon supported $Pt_{0.51}Au_{0.49}$ NPs do not take some *average* value but remain very close to their lengths in pure bulk Pt and Au. Thus when metal atoms of different dimensions ($Pt_{diameter} = 2.76(1)$ Å and $Au_{diameter} = 2.86(1)$ Å) are mixed together in NPs of an fcc-type structure the latter inevitably will have to distort locally to accommodate them. This may well explain why the rms atomic displacements in $Pt_{0.51}Au_{0.49}$ NPs are stronger than those in pure Pt and Au NPs. A similar effect has been observed in semiconductor alloys [22]. A question arises then how the different in size Pt and Au atomic species arrange themselves in a locally distorted fcc-type structure across the 4.5(3) nm NPs: forming a completely random or partially ordered alloy, or phase segregating in a core-shell type morphology as some theoretical predictions suggest [23–26]? To answer it structure models featuring NPs of real size (4.5 nm) and shape (spherical) that may incorporate
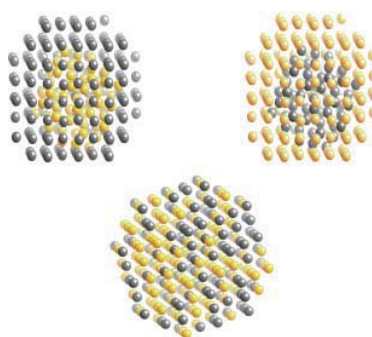

Fig. 5. Cartoons of Au_core-Pt_shell (left up), Pt_core-Au_shell (right up) and Au−Pt random alloy (down) NPs with an fcc-type structure. Au atoms are in yellow, Pt – in gray.

chemical inhomogeneities extending beyond a single unit cell of an fcc lattice have to be built and tested against the experimental PDF data in a manner described in Refs. [27, 28]. As can be seen in Fig. 5, the spatial arrangement of the Au and Pt atoms in the alloy and phase segregated model NPs is very different and so will be the respective Pt−Pt/Au and Au−Au atomic correlations. Hence, the models may be rigorously tested and refined against the Pt differential and Au−Au partial PDFs resulted from the present experiments. Such modeling studies are underway. Results will be reported elsewhere and used to verify the suggested strong relationship [10–14] between the chemical order-disorder effects and catalytic activity of PtAu NPs.

Conclusions

Coordination spheres related to a particular atomic species can be "highlighted" and others "dimmed" by exploiting high-energy resonant XRD, allowing to reveal the atomic arrangement in materials of limited structural coherence with both good spatial resolution and elemental specificity. This is a clear step forward in extending atomic PDFs analysis toward achieving a better sensitivity to sample's chemistry [29]. In particular, Au−Au and Pt−Pt bond lengths differing in only 0.1 Å are clearly revealed by conducting Pt *K* edge resonant XRD experiments on 4.5(3) nm carbon supported $Pt_{0.51}Au_{0.49}$ particles. Note that such a resolution is very hard to achieve by traditional high energy X-ray or neutron diffraction since it would require collecting data to wave vectors as high as 60 Å^{-1}. It may be difficult to be achieved by EXAFS experiments either since EXAFS data from species having absorption edges too close to each other, as it is the case with Pt and Au, are not trivial to disentangle [30]. Furthermore, differential and partial atomic PDFs are element specific and so can be very useful in exploring chemical order-disorder effects. In particular, they can be successful where high-angle-annular-dark field scanning transmission electron microscopy and other imaging techniques may fail [31] due to the very similar contrast (*i.e.* atomic/Z number) of the atomic species in the material studied. The resonant high-energy XRD and differential atomic PDFs technique requires a small amount of sample and works in various sample environments (*e.g.* supported NPs, samples in solu-

tion etc). Given this, and the number of high-energy synchrotron radiation facilities available worldwide, the technique should find widespread utility.

References

[1] T. Hahn, ed. in *International Tables for Crystallography*, Volume A, Kluwer, **2002**.

[2] C. Giacovazzo ed., in *Fundamentals of X-ray crystallography*, Oxford University Press, **1998**.

[3] H. P. Klug, L. E. Alexander, in *X-ray Diffraction Procedures for Polycrystalline and Amorphous Materials* John Wiley, New York, **1974**.

[4] T. Egami, S. J. L. Billinge in *Underneath the Bragg peaks*, Pergamon Press, **2003**.

[5] V. Petkov, *Materials Today* **2008**, *11,* 28.

[6] P. H. Fuoss, P. Eisenberger, W. K. Warburton, A. Bienenstock, *Phys. Rev. Lett*. **1981**, *46*, 1537.

[7] Y. Waseda, in *Novel Applications of Anomalous (Resonance) X-ray Scattering for Characterization of Disordered Materials* Springer, Berlin **1984**.

[8] V. Petkov, S. Shastri, *Phys. Rev. B* **2010**, *81*, 165428.

[9] V. Petkov, S. M. Selbach, M.-A. Einarsrud, T. Grande, S. D. Shastri, *Phys. Rev. Lett*. **2010**, *105*, 185501.

[10] J. Luo, M. M. Maye, V. Petkov, N. N. Kariuki, L. Wang, P. Njoki, D. Mott, Y. Lin, C. J. Zhong, *Chem. Mater.* **2005**, *17*, 3086.

[11] B. N. Wanjala, L. Luo, R. Loukrakpam, B. Fang, D. Mott, P. N. Njokki, M. Engelhard, H. R. Naslund, J. K. Wu, L. Wang, O. Malis, C. J. Zhong *Chem. Mat.* **2010**, *22*, 4282.

[12] B. Hammer and J. K. Norskov, *Nature* **1995**, *376*, 2238.

[13] B. R. Cuenya, *Thin Solid Films* **2010**, *518*, 3127.

[14] J. T. Miller, A. J. Kropf, Y. Zha, J. R. Regalbuto, L. Delannoy, C. Louis, E. Bus, N. Weiher, J. A. van Bokhoven, *J. Catal.* **2006**, *240*, 222.

[15] C. Xu, R. Wang, M. Chen, Y. Zhang, Y. Ding, *Phys. Chem. Chem. Phys.* **2010**, *12*, 239.

[16] S. D. Shastri, J. Almer, C. Ribbing, B. Cederström, *J. Synchrotron Radiat.* **2007**, *14*, 204.

[17] C. Wurden, K. Page, A. Llobet, C. E. White, Th. Proffen, *J. Appl. Cryst*. **2010**, *43*, 635.

[18] L. D. Marks, *Rep. Prog. Phys*. **1994**, *57*, 603.

[19] V. Petkov, Y. Peng, G. Williams, B. Huang, D. Tomalia, Y. Ren, *Phys. Rev. B* **2005**, *72*, 195402.

[20] C. L. Farrow, P. Juhás, J. W. Liu, D. Bryndin, E. S. Božin, J. Bloch, Th. Proffen, S. J. L. Billinge, *J. Phys.: Condens. Matter* **2007**, *19*, 335219.

[21] Y. Sun, L. Zhuang, J. L. Xinlin, P. Liu, *J. Am. Chem. Soc.* **2007**, *129*, 15465.

[22] V. Petkov, I.-K. Jeong, J. S. Chung, M. F. Thorpe, S. Kycia, S. J. L. Billinge, *Phys. Rev. Lett.* **1999**, *83*, 4089.

[23] S. Xiao, W. Hu, W. Luo, Y. Wu, X. Li, H. Deng, *Eur. Phys. J.* **2006**, *B 54*, 479.

[24] Z. Yang, X. Yang, Z. Xu, S. Liu, *Phys. Chem. Chem. Phys.* **2009**, *11*, 6249.

[25] I.-S. Park, K.-S. Lee, J.-H. Choi, H.-Y. Park, Y.-E. Sung, *J. Phys. Chem.* **2007**, *111*, 19126.

[26] L. Deng, W. Hu, H. Deng, S. Xiao, *J. Phys. Chem.* **2010**, *114*, 11026.

[27] V. Petkov, I. Moreels, Z. Hens, Y. Ren, *Phys. Rev. B* **2010**, *81*, 241304(R).

[28] K. Page, T. C. Hood, Th. Proffen, R. B. Neder, *J. Appl. Crystallogr.* **2011**, *44*, 327.

[29] Th. Proffen, V. Petkov, S. J. L. Billinge, T. Vogt, *Z. Kristallogr.* **2002**, *217*, 47.

[30] L. D. Menard, Qi Wang, J. H. Kang, A. J. Sealey, G. S. Girolami, X. Teng, A. I. Frenkel, R. G. Nuzzo, *Phys. Rev. B* **2009**, *80*, 064111.

[31] M. W. Small, S. I. Sanchez, L. D. Menard, J. H. Kang, A. I. Frenkel, R. G. Nuzzo, *J. Am. Chem. Soc*. **2011**, *133*, 3582.